ISSN (Print) 1226-1750
ISSN (Online) 2233-6656
Journal of Magnetics 31(3), 358-364 (2026) https://doi.org/10.4283/JMAG.2026.31.3.358

Impact of Fat-Suppression Strategy on Geometric Distortion in Diffusion-Weighted MRI: CHESS-Based versus Reverse-Gradient Approaches Using an ACR Phantom

Ho-Beom Lee[1] and Yong-Soo Han[2]*

[1]*Department of Radiological Science, Wonkwang University, 514, Iksan-daero, Iksan-si, Republic of Korea*
[2]*Department of Radiological Science, Hanlym Polytechnic University, Chuncheon 24210, Republic of Korea*

(Received 21 April 2026, Received in final form 12 July 2026, Accepted 13 July 2026)

This study aimed to quantitatively compare geometric distortion and image similarity among three diffusion-weighted imaging (DWI) techniques: conventional single-shot echo-planar imaging (SS-EPI) DWI, multi-shot echo-planar imaging (MS-EPI) DWI, and reverse-gradient fat suppression single-shot EPI (RGFS SS-EPI) DWI. An American College of Radiology (ACR) phantom was scanned on a 3.0T MRI system (Philips Ingenia CX) using a 32-channel head coil. T2-weighted turbo spin-echo (TSE) images served as the geometric gold standard. Geometric distortion was assessed by measuring dimensional differences between the DWI sequences and the T2 TSE reference, and the Structural Similarity Index (SSIM) was calculated to evaluate image quality. Results indicated that RGFS SS-EPI DWI demonstrated significantly reduced geometric distortion (1.84 ± 0.10%) compared to conventional SS-EPI DWI (4.19 ± 0.19%, $p < 0.001$) and MS-EPI DWI (2.12 ± 0.14%, $p < 0.05$). RGFS SS-EPI DWI yielded numerically higher SSIM values (0.863 ± 0.009) compared to MS-EPI (0.831 ± 0.012) and conventional SS-EPI (0.712 ± 0.018), although the difference between RGFS SS-EPI and MS-EPI was not statistically significant ($p = 0.082$). These findings suggest that RGFS SS-EPI DWI may improve geometric accuracy relative to conventional EPI-based techniques in a controlled phantom setting; however, further in vivo and multi-platform validation is required before direct clinical applicability can be assumed.

Keywords : diffusion-weighted imaging, reverse-gradient fat suppression, geometric distortion, single-shot EPI, ACR phantom, SSIM

1. Introduction

Diffusion-weighted imaging (DWI) has become an indispensable tool in modern neuroradiology, playing a critical role in the diagnosis of acute ischemic stroke, intracranial tumors, and demyelinating diseases. The ability of DWI to probe the microscopic random motion of water molecules provides unique contrast mechanisms that reflect tissue cellularity and integrity [1]. Currently, single-shot echo-planar imaging (SS-EPI) is the most widely used acquisition method for clinical DWI due to its rapid scan speed, which effectively freezes bulk physiological motion [2]. However, SS-EPI is inherently prone to severe artifacts, particularly geometric distortion and susceptibility artifacts at air-tissue interfaces, such as the temporal lobes and skull base. These distortions arise mainly from B0 field inhomogeneities and eddy currents accumulating over the long readout train associated with single-shot acquisition [3, 4].

To mitigate these limitations, multi-shot EPI (MS-EPI) techniques have been developed. By segmenting k-space into multiple shots, the effective echo spacing is reduced, thereby diminishing the accumulation of phase errors and resultant geometric distortions [5, 6]. While MS-EPI offers improved geometric fidelity compared to SS-EPI, it remains susceptible to some degree of distortion and requires sophisticated motion correction algorithms to prevent phase artifacts between shots [7, 8].

Recently, advanced EPI techniques with improved fat suppression and distortion control have been developed [9]. In this manuscript, spectral attenuated inversion recovery (SPAIR) and spectral presaturation with inversion recovery (SPIR) are used to denote conventional frequency-selective fat-suppression methods. The term reverse-gradient fat suppression (RGFS) is used for the single-shot EPI implementation based on slice-selection gradient

©The Korean Magnetics Society. All rights reserved.
*Corresponding author: Tel: +82-63-840-1236
Fax: +82-63-840-1082, E-mail: feel_love83@hanmail.net

© 2026 Journal of Magnetics

reversal (SSGR). On the Philips platform used in this study, this represents a vendor-specific implementation of the SSGR/LIPO concept, in which reversal of the slice-selection gradient polarity between the 90° excitation pulse and the 180° refocusing pulse shifts lipid signal relative to water so that fat is displaced partially outside the prescribed slice [10, 13]. Because this approach reduces reliance on B0/B1-sensitive spectral pre-pulses, it may shorten TE and improve geometric fidelity. The same principle can also be extended to multi-shot EPI and TSE-based diffusion imaging. However, quantitative phantom-based comparisons among conventional SS-EPI, MS-EPI, and RGFS SS-EPI DWI remain limited.

The purpose of this study was to quantitatively evaluate and compare the geometric distortion and structural similarity of three EPI-based DWI techniques—conventional SS-EPI DWI with SPAIR, MS-EPI DWI with SPAIR, and RGFS SS-EPI DWI—using an ACR standard phantom on a 3.0T MRI system. We hypothesized that RGFS SS-EPI DWI would demonstrate superior geometric accuracy and image similarity compared with conventional single-shot and multi-shot EPI techniques.

2. Materials and Methods

2.1. Phantom study

This study used a standard American College of Radiology (ACR) MRI phantom (cylindrical; diameter, 190 mm; length, 148 mm) [11]. The phantom was filled with a solution containing 10 mM $NiCl_2$ and 75 mM NaCl, designed to approximate the relaxation properties and conductivity of human tissue. To ensure thermal stability, the phantom was stored in the magnet room for 24 hours before imaging to allow temperature equilibration.

2.2. MR system and imaging protocols

All scans were performed on a 3.0T MRI system (Ingenia CX, Philips Healthcare, Best, The Netherlands) equipped with a 32-channel head coil. A T2-weighted turbo spin-echo (TSE) sequence was acquired to serve as the geometric "gold standard" reference, as TSE sequences are known to have negligible geometric distortion.

Three EPI-based diffusion-weighted sequences were acquired for comparison:

1) Conventional SS-EPI DWI: standard clinical single-shot echo-planar imaging with conventional SPAIR fat suppression; 2) MS-EPI DWI: multi-shot echo-planar imaging using 4 shots with conventional SPAIR fat suppression; and 3) RGFS SS-EPI DWI: single-shot echo-planar imaging using a reverse-gradient fat suppression method based on slice-selection gradient reversal (SSGR).

Detailed imaging parameters are summarized in Table 1. To ensure fair comparison, TR and TE values were matched as closely as possible across all DWI sequences. MS-EPI DWI required a slightly longer TE (95 ms) due to the additional time needed for multi-shot k-space segmentation and navigator echo acquisition.

2.3. Reverse-gradient fat suppression pulse sequence

Figure 1 illustrates the pulse sequence diagram for RGFS SS-EPI DWI. The key feature distinguishing RGFS SS-EPI DWI from conventional SS-EPI DWI is the slice-selection gradient reversal (SSGR)-based reverse-gradient fat suppression method. During the 90° excitation pulse, the slice-selection gradient (GSS) is applied with positive polarity, whereas during the 180° refocusing pulse the gradient polarity is reversed. Because the resonance frequency of fat is chemically shifted relative to water, this reversal changes the spatial refocusing

Table 1. Imaging parameters for T2 TSE, Conventional SS-EPI DWI, MS-EPI DWI, and RGFS SS-EPI DWI.

Parameter	T2 TSE Reference	SS-EPI DWI	MS-EPI DWI	RGFS SS-EPI DWI
TR (ms)	3000	4200	4200	4200
TE (ms)	80	62	95	62
FOV (mm)	256 × 256	256 × 256	256 × 256	256 × 256
Matrix	512 × 512	128 × 128	128 × 128	128 × 128
Slice thickness (mm)	5	5	5	5
b-value (s/mm²)	-	0, 1000	0, 1000	0, 1000
SENSE factor	-	2	2	2
Shots / NSA	-	1 / 1	4 / 1	1 / 1
Fat suppression	-	SPAIR	SPAIR	RGFS
Gradient mode	Default	Maximum	Maximum	Maximum

*TSE = turbo spin-echo, SPAIR = spectral attenuated inversion recovery, SPIR = spectral presaturation with inversion recovery, RGFS = reverse-gradient fat suppression.

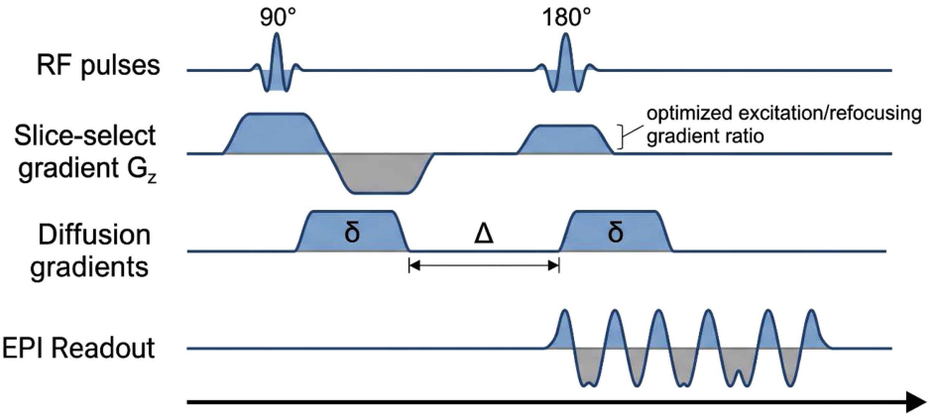


Fig. 1. (Color online) Schematic pulse sequence diagram of RGFS SS-EPI DWI. RGFS SS-EPI is a single-shot EPI sequence enhanced with reverse-gradient fat suppression. The key feature is reversal of the slice-selection gradient (GSS) polarity between the 90° excitation pulse and the 180° refocusing pulse. This SSGR-based approach spatially displaces and suppresses fat signal without additional spectral pre-pulses (e.g., SPAIR/SPIR). Following diffusion encoding with bipolar gradients (GDiff), the signal is acquired using a standard single-shot EPI readout train with alternating readout gradients (GRO) and phase-encoding blips (GPE), identical to conventional SS-EPI DWI.

position of lipid signal and displaces part of the fat magnetization outside the prescribed slice profile. As a result, substantial fat suppression can be achieved without additional spectral pre-pulses such as SPAIR or SPIR. In the present study, RGFS was implemented on a Philips 3.0T system as a vendor-specific SSGR/LIPO-type option rather than as a post-processing correction method. Following diffusion encoding, the signal is acquired using a standard single-shot EPI readout train identical to conventional SS-EPI DWI.

2.4. Image analysis

Geometric distortion was quantified using Slice 5 of the ACR phantom. Following the standard ACR geometric accuracy assessment, phantom diameters were measured in four directions (RL, AP, RD, and LD) on the b = 0 images of each DWI sequence, and the resulting geometric distortion values are summarized in Table 2. The orthogonal (RL and AP) and diagonal (RD and LD) measurements were selected to reflect the formal ACR large-geometry measurement scheme and to detect both direction-specific scaling errors and oblique deformation patterns. This approach was considered appropriate because EPI-related distortion can be most prominent along the phase-encoding direction while still propagating asymmetrically across the image.

$$\%GD = (|D_{measured} - D_{reference}| / D_{reference}) \times 100 \quad (1)$$

where $D_{measured}$ is the diameter measured on the DWI image and $D_{reference}$ is the corresponding diameter measured on the T2 TSE reference image.

In addition, the structural similarity index (SSIM) was calculated to assess image similarity between the b = 0 images of the DWI sequences and the T2 TSE reference image [12]. SSIM is a widely used metric for image quality assessment based on luminance, contrast, and structural information. It is defined as follows:

$$SSIM(x, y) = [l(x, y)] \cdot [c(x, y)] \cdot [s(x, y)] \quad (2)$$

where l(x, y), c(x, y), and s(x, y) denote the luminance, contrast, and structure comparison terms, respectively. In its simplified form, SSIM is expressed as:

$$SSIM(x, y) = [(2\mu x\mu y + C1)(2\sigma xy + C2)] / [(\mu x^2 + \mu y^2 + C1)(\sigma x^2 + \sigma y^2 + C2)] \quad (3)$$

where μx and μy are the mean intensities, σx^2 and σy^2 are the variances, σxy is the covariance, and C1 and C2 are stabilization constants. SSIM values range from -1 to 1, with 1 indicating perfect similarity. Before comparison, the T2 TSE images were downsampled to match the spatial resolution of the DWI images. Because T2-weighted and b = 0 DWI images inherently have different contrast mechanisms, SSIM in this study should be interpreted as a relative indicator of geometric/structural similarity rather than as a measure of absolute tissue-contrast equivalence. Region-of-interest analysis and image processing were performed using ImageJ (National Institutes of Health, Bethesda, MD, USA) and MATLAB (MathWorks, Natick, MA, USA).

2.5. Statistical analysis

Statistical analysis was performed using SPSS software (Version 26.0, IBM Corp., Armonk, NY). A one-way analysis of variance (ANOVA) followed by a post-hoc Tukey test was used to compare the means of geometric distortion and SSIM values among the three groups. Each sequence was acquired three times as independent scan repetitions, with the phantom repositioned before each repeat acquisition. For each acquisition, geometric measurements and SSIM were obtained once, and the acquisition-level values were treated as independent observations in the ANOVA and Tukey post-hoc analyses. A p-value of less than 0.05 was considered statistically significant. All measurements were repeated three times, and results are presented as Mean ± Standard Deviation (SD).

3. Results

The phantom diameter measurements and the resulting geometric distortion values are presented in Tables 2 and 3. Conventional SS-EPI DWI exhibited the highest mean geometric distortion at 4.19 ± 0.19%. MS-EPI DWI showed a significant reduction in distortion compared to conventional SS-EPI, with a mean of 2.12 ± 0.14%. RGFS SS-EPI DWI demonstrated the lowest geometric distortion among the three techniques, with a mean of 1.84 ± 0.10%. Statistical analysis revealed significant differences between conventional SS-EPI and both other methods ($p < 0.001$). The difference between MS-EPI and RGFS SS-EPI DWI was also statistically significant ($p < 0.05$), indicating that RGFS SS-EPI DWI, which enhances conventional single-shot EPI with reverse-gradient fat suppression, offers superior geometric fidelity.

SSIM values, which quantify structural similarity to the T2 TSE reference image, are summarized in Table 4. Representative phantom images are shown in Fig. 2. RGFS SS-EPI DWI achieved the numerically highest SSIM value (0.863 ± 0.009), followed by MS-EPI (0.831 ± 0.012), while conventional SS-EPI exhibited the lowest structural similarity (0.712 ± 0.018). Statistical analysis revealed significant differences between conventional SS-

Table 2. Phantom diameter measurements in four directions for the reference and DWI sequences (mean ± SD, mm).

Sequence	Geometric accuracy			
	RL	AP	RD	LD
T2WI	189.76 ± 0.05	190.21 ± 0.06	190.41 ± 0.14	190.73 ± 0.11
SS-EPI DWI	183.58 ± 0.35	184.61 ± 0.39	181.42 ± 0.61	183.45 ± 0.51
MS-EPI DWI	186.19 ± 0.23	185.85 ± 0.13	185.56 ± 0.31	184.60 ± 0.39
RGFS SS-EPI DWI	185.71 ± 0.52	185.15 ± 0.26	184.45 ± 0.42	183.85 ± 0.35

RL = right-to-left, AP = anterior-to-posterior, RD = right diagonal, and LD = left diagonal. Length values are presented as mean ± standard deviation (SD).

Table 3. Comparison of geometric distortion (%) among DWI sequences (mean ± SD).

Sequence	Geometric distortion (%)				
	RL	AP	RD	LD	Mean
SS-EPI DWI	4.21 ± 0.13	3.98 ± 0.14	4.45 ± 0.15	4.12 ± 0.18	4.19 ± 0.19[a]
MS-EPI DWI	2.14 ± 0.11	1.98 ± 0.13	2.31 ± 0.13	2.05 ± 0.15	2.12 ± 0.14[b]
RGFS SS-EPI DWI	1.87 ± 0.12	1.72 ± 0.12	1.95 ± 0.13	1.80 ± 0.10	1.84 ± 0.10[c]

Values are presented as mean ± standard deviation (SD). Values with different superscript letters are significantly different, whereas values sharing the same superscript letter are not significantly different ($p < 0.05$).

Table 4. Comparison of structural similarity index (SSIM) relative to the T2 TSE reference image (mean ± SD).

Sequence	SSIM	p-value		
		SS-EPI DWI	MS-EPI DWI	RGFS SS-EPI DWI
SS-EPI DWI	0.712 ± 0.018[a]	-	< 0.001	< 0.001
MS-EPI DWI	0.831 ± 0.012[b]	< 0.001	-	0.082 (NS)
RGFS SS-EPI DWI	0.863 ± 0.009[b]	< 0.001	0.082 (NS)	-

Values are presented as mean ± standard deviation (SD). Values sharing the same superscript letter are not significantly different, whereas values with different superscript letters are significantly different ($p < 0.05$, one-way ANOVA with post-hoc Tukey test). NS, not significant.

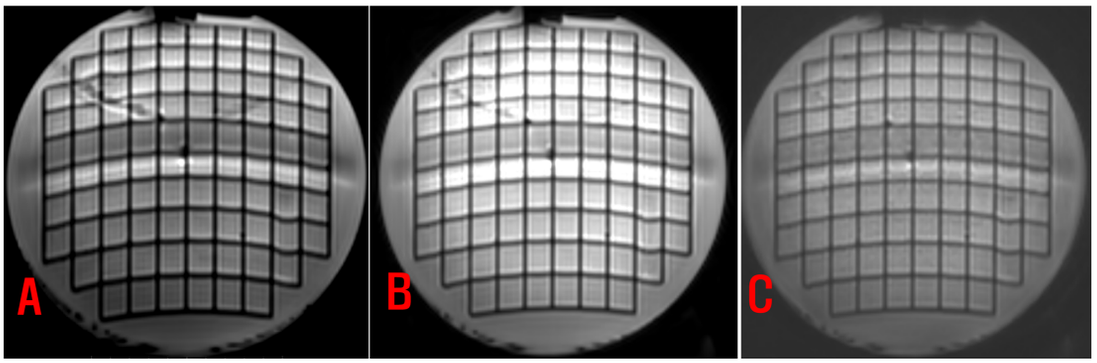


Fig. 2. (Color online) Representative phantom images obtained with conventional single-shot EPI DWI and single-shot EPI DWI with reverse-gradient fat suppression. Representative b = 0 images of the ACR phantom are shown for (A) conventional single-shot EPI DWI with SPAIR fat suppression, and (B) single-shot EPI DWI with reverse-gradient fat suppression. (C) multi-shot EPI DWI and SPAIR fat suppression.

EPI and both MS-EPI ($p < 0.001$) and RGFS SS-EPI ($p < 0.001$). However, the difference between MS-EPI and RGFS SS-EPI DWI did not reach statistical significance ($p = 0.082$). Although not statistically significant, RGFS SS-EPI DWI, which enhances conventional single-shot EPI with the reverse-gradient fat suppression technique, demonstrated a numerically higher SSIM value compared to MS-EPI, suggesting a trend toward improved structural fidelity.

4. Discussion

This study quantitatively demonstrated that RGFS SS-EPI DWI significantly outperforms conventional SS-EPI and MS-EPI techniques in terms of geometric accuracy. RGFS SS-EPI DWI is essentially conventional single-shot EPI enhanced with the reverse-gradient fat suppression technique. The superior performance of RGFS SS-EPI DWI can be attributed to several factors. First, the reverse-gradient fat suppression technique provides more uniform and robust fat suppression compared to conventional SPAIR or SPIR methods [10]. By reversing the slice-selection gradient polarity between the excitation and refocusing pulses, lipid signal is spatially displaced and suppressed without requiring additional pre-pulses, thereby shortening TE and reducing susceptibility to B0 and B1 inhomogeneities [13]. This improved fat suppression minimizes chemical shift artifacts that can contribute to apparent geometric distortion. Second, the elimination of spectrally selective fat suppression pulses reduces overall SAR and allows for more optimal gradient timing, potentially improving spatial encoding fidelity.

4.1. Mechanisms of Geometric Distortion in EPI-Based DWI

The geometric distortion observed in EPI-based DWI arises from several interrelated factors. First, B0 field inhomogeneity causes local variations in resonance frequency, leading to pixel shifts in the phase-encoding direction. The magnitude of this shift is proportional to the echo spacing and inversely proportional to the receiver bandwidth in the phase-encoding direction [3]. In SS-EPI, the entire k-space is traversed in a single excitation, resulting in echo trains exceeding 50-100 ms, during which substantial phase errors accumulate. Second, eddy currents induced by rapid gradient switching create time-varying magnetic fields that further distort the acquired signal [14]. These eddy currents have both short-lived (< 5 ms) and long-lived (> 50 ms) components, with the latter being particularly problematic for diffusion imaging due to the strong diffusion-encoding gradients.

Our results showed that while MS-EPI significantly reduced distortion compared to conventional SS-EPI (by approximately 50%), it did not reach the geometric fidelity of RGFS SS-EPI DWI. MS-EPI reduces the effective echo spacing by segmenting k-space into multiple shots (typically 2-4 shots), which mitigates phase accumulation errors [6, 15]. However, MS-EPI is vulnerable to inter-shot phase inconsistencies caused by bulk motion, cardiac pulsation, and respiratory motion, requiring sophisticated navigator-based correction algorithms [5, 7]. The superior performance of RGFS SS-EPI DWI may be attributed to the combination of optimized gradient timing and the elimination of B0-sensitive fat suppression pre-pulses, which together reduce sources of geometric distortion. Additionally, RGFS SS-EPI DWI

maintains the fast acquisition speed of conventional single-shot EPI while achieving improved geometric accuracy through the RGFS technique.

4.2. Advantages of RGFS SS-EPI DWI: Reverse-Gradient Fat Suppression

RGFS SS-EPI DWI utilizes a slice-selection gradient reversal (SSGR)-based reverse-gradient fat suppression method to achieve robust fat suppression without requiring additional frequency-selective pre-pulses such as SPAIR or SPIR [10, 13]. By reversing the polarity of the slice-selection gradient between the excitation and refocusing pulses, lipid signal is spatially displaced and subsequently suppressed. This approach eliminates time-consuming and SAR-intensive spectral fat suppression pulses, may shorten TE, and is less sensitive to B0 and B1 field inhomogeneities than conventional SPAIR/SPIR methods. These characteristics likely contribute to the reduced geometric distortion observed in this study.

Importantly, the RGFS principle is not limited to single-shot EPI acquisitions. It can also be applied to multi-shot EPI and Turbo Spin Echo (TSE) sequences, enabling distortion-free TSE-based DWI with robust fat suppression [13]. TSE-based DWI inherently provides superior geometric fidelity compared to any EPI technique by refocusing static field inhomogeneities at each echo through 180-degree refocusing pulses. When combined with the reverse-gradient fat suppression technique, TSE-based RGFS DWI may provide a favorable solution for applications requiring high geometric accuracy, such as spinal cord diffusion imaging, head and neck imaging, and musculoskeletal DWI. While TSE-based RGFS DWI has longer acquisition times than EPI-based techniques (including both conventional SS-EPI and RGFS SS-EPI) and is more susceptible to motion artifacts, it may provide superior geometric fidelity in scenarios where patient motion can be controlled.

The SSIM analysis provided additional insight into structural preservation. While RGFS SS-EPI DWI achieved the numerically highest SSIM value (0.863 ± 0.009), the difference compared to MS-EPI (0.831 ± 0.012) was not statistically significant ($p = 0.082$). This suggests that both RGFS SS-EPI and MS-EPI DWI preserve structural information with relatively high fidelity compared to conventional SS-EPI. SSIM takes into account luminance, contrast, and structural similarities, providing a more comprehensive assessment than simple pixel-wise metrics. The trend toward higher SSIM values in RGFS SS-EPI DWI may be clinically relevant for precise lesion localization and accurate co-registration with anatomical images [16]. Moreover, the impact of distortion correction may extend beyond visually obvious regions, affecting overall image fidelity and diffusion-based interpretation [17]. In clinical scenarios involving the skull base, orbits, or temporal bones, where B0 inhomogeneity-related artifacts can degrade image quality in conventional DWI, RGFS SS-EPI DWI could provide a robust alternative [18]. Furthermore, RGFS SS-EPI DWI may be particularly beneficial in regions where conventional fat suppression techniques fail, such as in patients with poor B0 shimming or in anatomical areas with complex tissue interfaces.

4.3. Clinical Implications and Future Directions

The improved geometric fidelity of RGFS SS-EPI DWI has several important clinical implications [21]. First, accurate lesion localization is critical for treatment planning in neurosurgery and radiation oncology [16]. Geometric distortions in conventional DWI can lead to errors of several millimeters, which may result in incorrect targeting or margin delineation [19, 20]. Second, the high structural similarity of RGFS SS-EPI DWI to anatomical T2-weighted images facilitates automated co-registration and fusion with other imaging modalities, such as CT or PET. Third, reduced susceptibility artifacts enable diagnostic imaging in anatomical regions that are traditionally challenging for DWI, including the brainstem, cerebellopontine angle, and sella turcica [22, 23].

While RGFS SS-EPI DWI demonstrated superior geometric accuracy in this phantom study, clinical validation is necessary. The improved fat suppression provided by the RGFS technique may be particularly beneficial in anatomical regions with significant lipid content, such as the orbits, skull base, and spine, where conventional fat suppression methods often fail. Future studies should evaluate RGFS SS-EPI DWI performance in vivo, particularly in comparison to TSE-based RGFS DWI, which offers even greater geometric fidelity at the cost of longer scan times and increased motion sensitivity [24]. The versatility of the RGFS technique—applicable to single-shot EPI, multi-shot EPI, and TSE acquisitions—makes it a valuable tool for tailoring DWI protocols to specific clinical scenarios. For time-critical applications such as acute stroke imaging, RGFS SS-EPI DWI provides an optimal balance between speed and geometric accuracy. For applications where geometric precision is paramount and motion can be controlled, TSE-based RGFS DWI may be preferable.

This study has several limitations. First, it was a phantom-only study, and the ACR phantom cannot reproduce physiological motion, pulsation, flow, complex tissue susceptibility interfaces, or true lesion conspicuity. Second, all data were acquired on a single 3.0T Philips

MRI system using a vendor-specific implementation of RGFS; therefore, the results may not be directly generalizable to other scanner platforms, field strengths, gradient performances, or sequence implementations. Third, the protocols were optimized for our institution, and parameter changes such as b-value, diffusion direction number, SENSE factor, and gradient mode may alter both distortion behavior and image similarity metrics. Finally, we did not directly compare RGFS with TSE-based diffusion acquisitions or with other contemporary distortion-correction strategies. These points should be considered when interpreting the present findings.

5. Conclusion

In conclusion, RGFS SS-EPI DWI demonstrated significantly reduced geometric distortion compared with conventional SS-EPI and MS-EPI DWI in this controlled phantom model. Although RGFS SS-EPI DWI showed the highest mean SSIM value, the difference relative to MS-EPI was not statistically significant, suggesting comparable structural preservation between these two techniques under the present experimental conditions. The findings support RGFS as a technically promising fat-suppression strategy for improving geometric fidelity in EPI-based diffusion imaging.

Acknowledgments

This research was supported by the research fund of Wonkwang University in 2026.

References

[1] D. Le Bihan, E. Breton, D. Lallemand, P. Grenier, E. Cabanis, and M. Laval-Jeantet, Radiology **161**, 401 (1986).
[2] M. E. Moseley, Y. Cohen, J. Mintorovitch, L. Chileuitt, H. Shimizu, J. Kucharczyk, M. F. Wendland, and P. R. Weinstein, Magn. Reson. Med. **14**, 330 (1990).
[3] P. Jezzard and R. S. Balaban, Magn. Reson. Med. **34**, 65 (1995).
[4] J. M. Treiber, N. S. White, T. C. Steed, H. Bartsch, D. Holland, N. Farid, C. R. McDonald, B. S. Carter, A. M. Dale, and C. C. Chen, PLoS One **11**, e0152472 (2016).
[5] D. A. Porter and R. M. Heidemann, Magn. Reson. Med. **62**, 468 (2009).
[6] S. J. Holdsworth, S. Skare, R. D. Newbould, R. Guzmann, N. H. Blevins, and R. Bammer, Eur. J. Radiol. **65**, 36 (2008).
[7] R. Bammer, Eur. J. Radiol. **45**, 169 (2003).
[8] N. K. Chen, A. Guidon, H. C. Chang, and A. W. Song, NeuroImage **72**, 41 (2013).
[9] T. Sjoholm, P. J. Bostrom, E. G. H. W. van der Meij, J. W. van der Linden, and H. Ahlstrom, Sci. Rep. **12**, 11463 (2022).
[10] K. Zhang, H. Wu, and X. Zhang, J. Magn. Reson. Imaging **48**, 123 (2018).
[11] T. M. Ihalainen, N. Lonnroth, J. I. Peltonen, J. Uusi-Simola, and M. Kortesniemi, Acta Oncol. **50**, 966 (2011).
[12] Z. Wang, A. C. Bovik, H. R. Sheikh, and E. P. Simoncelli, IEEE Trans. Image Process. **13**, 600 (2004).
[13] Z. Nagy and N. Weiskopf, Magn. Reson. Med. **60**, 1256 (2008).
[14] S. Skare and R. Bammer, Magn. Reson. Med. **64**, 1158 (2010).
[15] S. J. Holdsworth, S. Skare, R. D. Newbould, and R. Bammer, Magn. Reson. Med. **62**, 1629 (2009).
[16] H. Kavaluus, K. Nousiainen, S. Kaijaluoto, J. Kangasniemi, and T. Seppala, Phys. Imaging Radiat. Oncol. **17**, 58 (2021).
[17] J. P. Begnoche, K. G. Schilling, B. D. Boyd, and B. A. Landman, Magn. Reson. Imaging **92**, 1 (2022).
[18] T. Sakai, K. Ota, and H. Imai, Proc. Int. Soc. Magn. Reson. Med. **31**, 2544 (2023).
[19] H. B. Lee and Y. S. Han, J. Magn. **28**, 112 (2023).
[20] N. S. White, G.-Y. Kim, V. Moiseenko, C. R. McDonald, N. Farid, H. Bartsch, J. Kuperman, R. Karunamuni, D. Marshall, D. Holland, P. Sanghvi, D. R. Simpson, A. J. Mundt, A. M. Dale, and J. A. Hattangadi-Gluth, Pract. Radiat. Oncol. **6**, e319 (2016).
[21] N. F. Grauhan, N. Grünebach, L. Brockstedt, A. Sanner, T. Feiweier, V. Schöffling, M. A. Brockmann, and A. E. Othman, Clin. Neuroradiol. **34**, 85 (2024).
[22] S. Ito, S. Okuchi, Y. Fushimi, S. Otani, K. P. Wicaksono, A. Sakata, K. K. Miyake, H. Numamoto, S. Nakajima, H. Tagawa, M. Tanji, N. Sano, H. Kondo, R. Imai, T. Saga, K. Fujimoto, Y. Arakawa, and Y. Nakamoto, Eur. Radiol. Exp. **8**, 28 (2024).
[23] N. Kashiwagi, M. Sakai, A. Nakamoto, H. Takahashi, Y. Isogawa, Y. Suzuki, S. Yamada, M. Tomiyama, K. Nakanishi, and N. Tomiyama, J. Comput. Assist. Tomogr. **49**, 140 (2025).
[24] H. Bai, Z. Zhou, K. Dai, W. Shen, H. Chen, and Z. Zhang, Quant. Imaging Med. Surg. **16**, 214 (2026).